

## RESEARCH ARTICLE

# Weighted model-based optoacoustic reconstruction for partial-view geometries

Marwan Muhammad<sup>1,2</sup>  | Jaya Prakash<sup>1,2</sup>  | Evangelos Liapis<sup>1,2</sup> |  
Vasilis Ntziachristos<sup>1,2,3</sup> | Dominik Jüstel<sup>1,2,4\*</sup>

<sup>1</sup>Institute of Biological and Medical Imaging, Helmholtz Zentrum München, Neuherberg, Germany

<sup>2</sup>Chair of Biological Imaging at the Center for Translational Cancer Research (TranslaTUM), School of Medicine, Technical University of Munich, Munich, Germany

<sup>3</sup>Munich Institute of Robotics and Machine Intelligence (MIRMI), Technical University of Munich, Munich, Germany

<sup>4</sup>Institute of Computational Biology, Helmholtz Zentrum München, Neuherberg, Germany

## \*Correspondence

Dominik Jüstel, Chair of Biological Imaging at the Center for Translational Cancer Research (TranslaTUM), School of Medicine, Technical University of Munich, 81675, Munich, Germany.  
Email: dominik.juestel@tum.de

## Present address

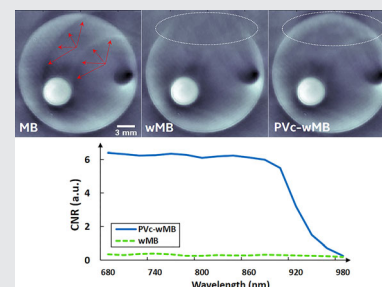
Marwan Muhammad, Graduate Center BioEngineering (GCB), Munich Institute of Biomedical Engineering (MIBE), Technical University of Munich, Garching b. München, Germany

Jaya Prakash, Indian Institute of Science, Bengaluru, Karnataka, India

Evangelos Liapis, Hackensack Meridian School of Medicine, Center for Discovery and Innovation, Nutley, NJ, USA

## Abstract

Acoustic heterogeneities in biological samples are known to cause artifacts in tomographic optoacoustic (photoacoustic) image reconstruction. A statistical weighted model-based reconstruction approach was previously introduced to mitigate such artifacts. However, this approach does not reliably provide high-quality reconstructions for partial-view imaging systems, which are common in preclinical and clinical optoacoustics. In this article, the capability of the weighted model-based algorithm is extended to generate optoacoustic reconstructions with less distortions for partial-view geometry data. This is achieved by manipulating the weighting scheme based on the detector geometry. Using partial-view optoacoustic tomography data from a tissue-mimicking phantom containing a strong acoustic reflector, tumors grafted onto mice, and a mouse brain with intact skull, the proposed partial-view-corrected weighted model-based algorithm is shown to mitigate reflection artifacts in reconstructed images without distorting structures or boundaries, compared with both conventional model-based and the weighted model-based algorithms. It is also demonstrated that the partial-view-corrected weighted model-based algorithm has the additional advantage of suppressing streaking artifacts due to the partial-view geometry itself in the presence of a very strong optoacoustic chromophore. Due to its enhanced performance, the partial-view-corrected weighted model-based algorithm may prove useful for improving the quality of partial-view multispectral optoacoustic tomography, leading to enhanced visualization of functional parameters such as tissue oxygenation.



**Abbreviations:** BGD, background; MSOT, multispectral optoacoustic tomography; OA, optoacoustic; PVC, partial-view-corrected; ROI, region of interest; sO<sub>2</sub>, oxygen saturation; wMB, weighted model-based

This is an open access article under the terms of the Creative Commons Attribution License, which permits use, distribution and reproduction in any medium, provided the original work is properly cited.

© 2022 The Authors. *Journal of Biophotonics* published by Wiley-VCH GmbH.

**Funding information**

Alexander von Humboldt-Stiftung; FP7  
People: Marie-Curie Actions, Grant/  
Award Number: 605162; Horizon 2020  
Framework Programme, Grant/Award  
Number: 694968

**KEYWORDS**

acoustic heterogeneities, optoacoustic (photoacoustic) imaging, partial-view correction, streaking artifacts, weighted model-based reconstruction

**1 | INTRODUCTION**

Most OA reconstruction algorithms assume that the sample under investigation is acoustically homogeneous and perfectly matched to the coupling medium between the sample and the acoustic detectors [1–3]. However, in in vivo imaging cases, the propagation of OA waves is distorted due to acoustic heterogeneities inside the imaged sample. For example, lungs, bones and other tissues with high acoustic mismatch to surrounding tissues can induce strong acoustic reflections, scattering or speed-of-sound variation artifacts in reconstructed OA images [4, 5], reducing the overall image fidelity [6]. Acoustic heterogeneities can also contribute to the appearance of artifactual negative values in the reconstructed images [7] with adverse effects on spectral unmixing and functional OA imaging [8].

Different approaches have been introduced to account for the effects of acoustic heterogeneities. One method incorporated a higher-order geometrical acoustics approximation in the reconstruction algorithm to account for the time-shift of OA signals caused by variations in the speed of sound [9]. Another finite-element reconstruction algorithm was based on the Helmholtz-like OA wave equation in the frequency domain to increase the efficiency of computing the OA inverse problem solution in the presence of heterogeneities [10]. Another strategy, previously introduced by colleagues of our research group, was based on a statistical approach to account for artifacts due to acoustic heterogeneities [11]. The main idea of this approach is to weight the contribution of the detected OA signals during the reconstruction by the probability that they are distorted on their propagation path to the detector, assuming that the closer an OA signal generator is to the detector, the lower the distortion of this signal will be. This statistical approach was shown to be generally effective at mitigating artifacts due to acoustic heterogeneities in reconstructions of in vivo scans [12]. Initially developed for the back-projection algorithm, this statistical approach was later adapted for MB reconstruction [12] in order to provide more accurate anatomical reconstructions and quantitation of the optical absorption distribution [13]. The MB implementation of this statistical approach, to which we refer below as “wMB”, resulted in reconstructions containing less noise and artifacts [12] compared with reconstructions

that utilized only the first half (timewise) of the acquired data for each detector [14].

Despite the promising potential of the wMB algorithm to reduce artifacts due to acoustic heterogeneities in full-view cross-sectional coverage [11, 12], when it was applied to PV data, in which the detection geometry does not cover the entire sample, it caused noticeable distortion at areas of the image that were not well covered by the tomographic projections [15]. In this study, we hypothesized that by suitably manipulating the weighting scheme of the wMB approach to take into account the PV detection geometry, we could enhance the quality of PV reconstructions using the same weighting principle. Such development can be particularly useful for clinical scanners operating in handheld mode, since they collect data over limited projection angles [16]. To achieve such improved performance, we developed a “PV-corrected” version of the wMB algorithm (PVC-wMB) based on manipulating the decreasing probabilistic weighting particularly for detectors which are geometrically on the opposing side of the empty section of the detection circular aperture. The performance of the proposed modified algorithm was examined on a tissue-mimicking phantom and in vivo datasets. It produced reconstructions with fewer distortions, while maintaining the mitigation of reflection artifacts, and sharper images compared with conventional MB and the unmodified wMB reconstructions, thus improving the quality of both anatomical images and quantitative oxygenation maps. We further demonstrated that the PVC-wMB algorithm can in some cases suppress streaking artifacts that arise due to the PV geometry itself (i.e., not only due to acoustic heterogeneities) in the presence of a very strong OA absorber.

**2 | MATERIALS AND METHODS****2.1 | Theoretical foundation****2.1.1 | MB reconstruction**

The OA pressure that is generated and propagated in an OA sample in response to optical excitation is described by the following equation [3]:

$$p(\mathbf{r}, t) = \frac{\Gamma}{4\pi c} \frac{\partial}{\partial t} \int_{S_{et}(\mathbf{r})} \frac{H(\mathbf{r}')}{|\mathbf{r} - \mathbf{r}'|} dS(\mathbf{r}'), \quad (1)$$

where  $p(\mathbf{r}, t)$  is the OA pressure at a certain location  $\mathbf{r}$  and time  $t$ ;  $\Gamma$  is the Grueneisen parameter;  $c$  is the speed of sound;  $H$  is the energy absorbed per unit volume;  $S_{ct}(\mathbf{r})$  is the surface of a sphere centered at  $\mathbf{r}$  with radius  $ct$ .

The conventional MB reconstruction algorithm is based on discretization of the OA forward model in Equation (1), provided that thermal confinement conditions are applicable [13]. Such discretization can be represented as:

$$p(\mathbf{r}_i, t_j) = \sum_{k=1}^N a_k^{ij} H(\mathbf{r}'_k), \quad (2)$$

where  $H$  is evaluated at pixel locations  $\mathbf{r}'_k$  on the discrete grid on which the reconstruction is computed;  $a_k^{ij}$  are coefficients encoding the physical parameters in Equation (1) that describe the propagation of OA pressure waves;  $N$  is the number of pixels. Equation (2) can be represented as a linear system of equations in the following matrix form:

$$\mathbf{p} = \mathbf{A}_M \mathbf{H}, \quad (3)$$

where  $\mathbf{A}_M$  is called the model matrix;  $\mathbf{p}$  and  $\mathbf{H}$  are the vector forms of  $p(\mathbf{r}_i, t_j)$  and  $H(\mathbf{r}'_k)$ , respectively.

The inversion process (i.e., the calculation of  $\mathbf{H}$ ) is performed by minimizing the mean squared difference between the pressure  $\mathbf{p}$  predicted by the model and the measured pressure  $\mathbf{p}_m$  according to the following formula: [13]

$$\mathbf{H} = \underset{\mathbf{H}}{\operatorname{argmin}} (\|\mathbf{p}_m - \mathbf{A}_M \mathbf{H}\|^2 + \lambda^2 \|\mathbf{L} \mathbf{H}\|^2), \quad (4)$$

where  $\lambda$  is the regularization parameter, and  $\mathbf{L}$  is a matrix that usually corresponds to a high-pass spatial filter applied to the result of the reconstruction (imposing a smoothness constraint on the solution) [17]. Regularization is particularly required in the case of PV geometries because the given inverse problem is ill-posed for such geometries.

### 2.1.2 | wMB reconstruction

A weighting technique was previously introduced to the conventional MB algorithm to mitigate artifacts in OA reconstructions due to the presence of acoustic heterogeneities in the imaged sample [12]. The basic principle behind this technique is the following: in the case of no prior knowledge about the distribution of optical absorbers or acoustic heterogeneities in the sample, it

can be generally assumed that the further the location from which an OA signal is propagating to a detector, the less probable it is that this signal propagates directly to that specific detector. That is; if strong acoustic heterogeneities are likely to be present in the propagation path, there is a probability that any measured signal could have been already distorted during its propagation before reaching a detector that is far from the source of this signal.

To further explain this principle, we assume an area  $A$  is manually chosen to encircle all optical absorbers and acoustic heterogeneities (light blue area in Figure 1) in an imaged sample. The probability  $P_{\mathbf{r}}^i(t_j)$  of detecting a reflected or scattered wave at the transducer at position  $i$  and at time  $t_j$  was given by the formula: [11]

$$P_{\mathbf{r}}^i(t_j) = \int_{A_{ij}} P_{\mathbf{r}}^i(t_j | \mathbf{r}') f_E(\mathbf{r}') d\mathbf{r}', \quad (5)$$

where  $f_E(\mathbf{r}')$  is the probability density function that an energy differential is absorbed at location  $\mathbf{r}'$ ;  $P_{\mathbf{r}}^i(t_j | \mathbf{r}')$  is the conditional probability that a reflected or scattered wave with unit amplitude is detected at the instant  $t_j$ , given that all the optical energy is absorbed at  $\mathbf{r}'$ ;  $A_{ij}$  is the intersection of  $A$  and the circle centered at transducer  $i$  with radius  $ct_j$ . Such intersection is chosen as the integral support in order to exclude regions where definitely no acoustic heterogeneities exist (for example, the water path between the imaged sample and the detector). The probability  $P_{\mathbf{r}, dist}^i(t_j | \mathbf{r}')$  that the wave, detected at the  $i^{\text{th}}$  transducer at instant  $t_j$ , is distorted (hence the subscript *dist*) by a reflected or scattered wave is proportional to  $P_{\mathbf{r}}^i(t_j | \mathbf{r}')$ , and was approximated as

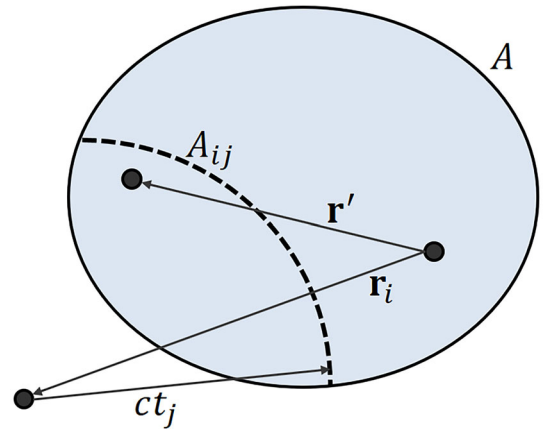


**FIGURE 1** Illustration of the weighting approach in the original wMB algorithm. The area  $A$  contains all optical absorbers and acoustic heterogeneities. The area  $A_{ij}$  is the intersection of  $A$  and the circle centered at the transducer located at  $\mathbf{r}_i$  with radius  $ct_j$

$$P_{\mathbf{r},dist}^i(t_j) \approx \min\left(1, \omega \left(\frac{A_{ij}}{A}\right)\right), \quad (6)$$

where  $\omega$  is a heuristic parameter [11]. Hence, the probability  $P_d^i(t_j)$  that the signal detected by the  $i^{\text{th}}$  transducer at instant  $t_j$  has undergone a “direct” propagation (hence the subscript  $d$ ) is given by

$$P_d^i(t_j) \triangleq 1 - P_{\mathbf{r},dist}^i(t_j) = \max\left(0, 1 - \omega \left(\frac{A_{ij}}{A}\right)\right). \quad (7)$$

The main idea of the wMB reconstruction approach is to incorporate  $P_d^i(t_j)$  as a weighting term (representing the acoustic heterogeneity of the sample) in the forward propagation model before attempting to solve the inverse acoustic problem. That is; Equation (2) is modified according to this approach to

$$P_d^i(t_j)p(\mathbf{r}_i, t_j) = P_d^i(t_j) \sum_{k=1}^N a_k^{ij} H(\mathbf{r}'_k). \quad (8)$$

Similarly, the matrix form in Equation (3) is modified to

$$\mathbf{Wp} = \mathbf{W}\mathbf{A}_M\mathbf{H}, \quad (9)$$

where  $\mathbf{W}$  is a diagonal matrix containing the elements of  $P_d^i(t_j)$  on its diagonal.

It was shown that this wMB technique mitigates artifacts due to acoustic reflections in tissue-mimicking phantoms and in vivo cases for full-view cross-sectional geometries [11, 12]. For PV geometries however, due to the nature of the weighting scheme, areas in the image that are not fully covered by the detection geometry tend to be severely underweighted. Consequently, the reconstruction at these areas is distorted.

To further illustrate the underweighting problem, we assume that the PV imaging domain can be represented by the region covered by the 2D detection arc  $\partial D$  as in Figure 2a. This circular detection arc is covering only  $270^\circ$  of the 2D imaging plane to resemble the preclinical MSOT system used in this study. The weighting function  $P_d^i(t_j)$  can be graphically represented as in Figure 2b. For the wMB algorithm, the signal at detector  $i$  is multiplied by the weight  $P_d^i(t_j)$ . Specifically for detectors in the section  $\partial D_u$  (indicated by the red bold section of the detection arc  $\partial D$ ), this weighting approach underweights the

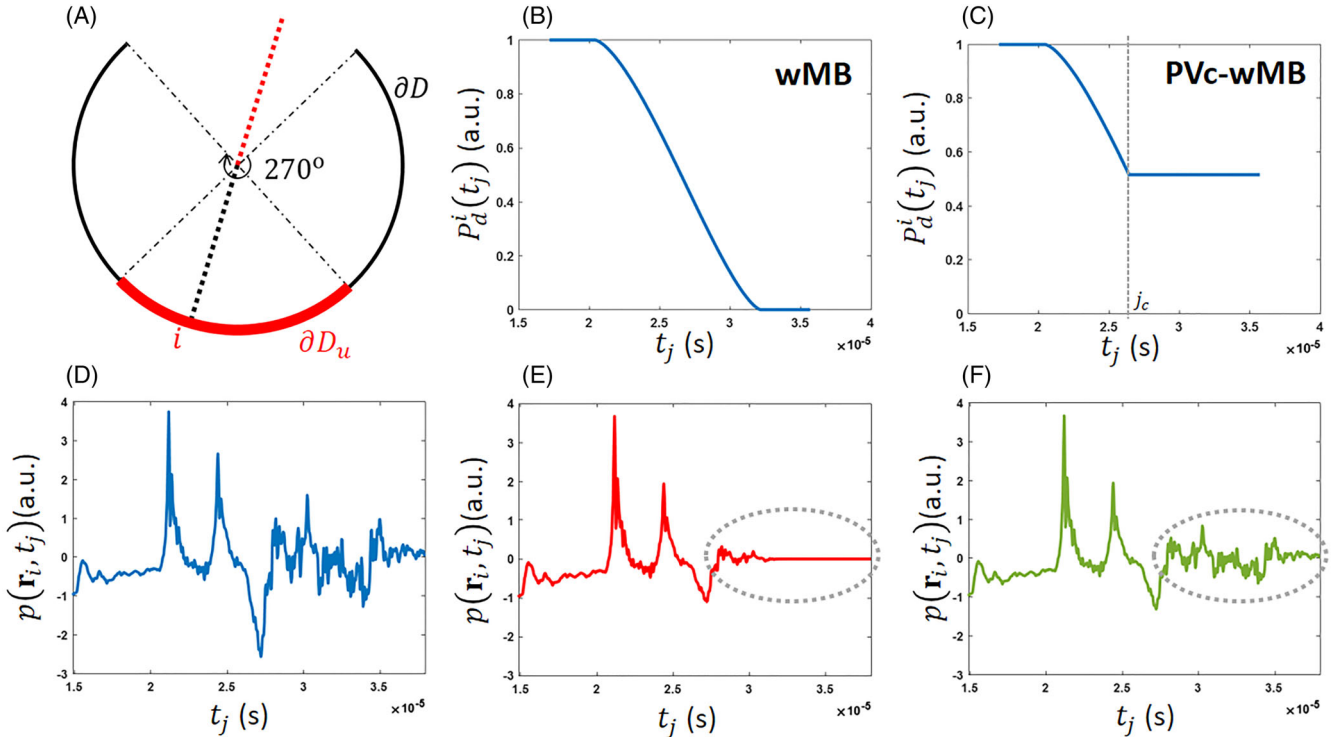


**FIGURE 2** Illustrative figures for the theoretical basis of the proposed PVc-wMB algorithm. (a) A diagram of the  $270^\circ$ -PV detection geometry investigated in this article. (b,c)  $P_d^i(t_j)$  plots for transducer  $i$  for (b) the wMB, and (c) the proposed PVc-wMB reconstruction algorithms. (d) Detected OA signal for transducer  $i$  with no weighting (used in the conventional MB reconstruction). (e–f) The same detected signal for transducer  $i$  in (d) after being weighted by  $P_d^i(t_j)$  for (e) the wMB, and (f) the proposed PVc-wMB algorithms

detected samples indicated by the red dotted segment for transducer  $i$  (corresponding spatially to OA signals originating at locations farther than the center of the detection circular aperture  $\partial D$ ). Consequently, image parts corresponding to these underweighted samples are relatively distorted in the final reconstruction.

This underweighting can be justified due to two reasons. First, there are no detectors on the opposite side to  $\partial D_u$  to compensate for such underweighting. Second, and commonly for such OA scanners, the acoustic detectors and illumination sources are on the same circular aperture (i.e., both the detection and illumination geometries are the same). This leads to a relatively weaker illumination in areas not fully covered by the geometry, aggravating the underweighting problem.

### 2.1.3 | PVC-wMB reconstruction

To circumvent the underweighting problem of the wMB algorithm for transducers in  $\partial D_u$ , we introduce a modification to the weighting function  $P_d^i(t_j)$  that takes into account the PV geometry. In principle, we manipulate a part of  $P_d^i(t_j)$  to counteract this underweighting effect. That is; we propose to modify Equation (7) particularly for the affected detectors to become:

$$P_d^i(t_j) = \begin{cases} \max\left(0, 1 - \omega\left(\frac{A_{ij}}{A}\right)\right), & j < j_c \\ 1 - \omega\left(\frac{A_{ij_c}}{A}\right), & j \geq j_c \end{cases}, \quad (10)$$

where the instant  $j_c$  can be chosen to correspond spatially to the center of the detection circular aperture  $\partial D$ . This value for  $j_c$  was also the choice for the half-time reconstruction approach published before [14]. This choice is reasonable because the imaged sample is almost always placed in the center of the scanning aperture in order to maintain the homogeneity of both illumination and detection. For transducers in  $\partial D_u$ , this modification changes the temporal profile of the weighting function  $P_d^i(t_j)$  from Figure 2b to Figure 2c.

To demonstrate how the weighting term  $P_d^i(t_j)$  affects the temporal profile of the detected signals for detectors in  $\partial D_u$  for both the wMB and PVC-wMB algorithms, we assume that the raw detected signal by transducer  $i$  in Figure 2a is as shown in Figure 2d. If the original wMB weighting (without PVC; as in Equation (7) and Figure 2b) is applied to this raw signal, the signal changes to the curve shown in Figure 2e. However, if the same weighting, but with the proposed PVC (as in Equation (10)

and Figure 2c), is applied to the raw signal, it changes to the curve shown in Figure 2f. It can be noticed that the detected samples corresponding spatially to OA signals originating at locations farther than the center of the detection circular aperture (indicated by the dotted gray ellipse) are much less flattened in Figure 2f compared with Figure 2e. This demonstrates how incorporating the proposed PVC in the wMB algorithm can alleviate the aforementioned underweighting issue in PV OA imaging scenarios.

## 2.2 | Experimental setup and datasets

In order to evaluate the performance of the proposed PVC-wMB reconstruction algorithm, both phantom and in vivo experiments were carried out using a commercial preclinical MSOT scanner (MSOT256-TF, iTheraMedical GmbH, Munich, Germany). In this system, a wavelength-tunable Nd:Yag pump optical parametric oscillator-based laser provides pulsed excitation between 680 and 980 nm with a pulse width of about 10 ns, repetition rate of 10 Hz, and per-pulse energy of about 90 mJ. The optical output is shaped by means of a fiber bundle to provide a 2D ring-like cross-sectional illumination. The acoustic detection part of this system consists of a 256-element concave array of cylindrically focused piezoelectric transducers with a central frequency of 5 MHz, a radius of curvature of 40 mm and an angular coverage of approximately  $270^\circ$  (hence the PV problem) [18, 19].

### 2.2.1 | Phantom dataset

A tissue-mimicking phantom was prepared to illustrate the nature of the artifacts produced due to the presence of a strong acoustic heterogeneity. To achieve this purpose, a cylindrically shaped absorbing inclusion and a hollow cylindrical cavity are included in the phantom. The optical absorption of the absorbing inclusion was obtained by adding India ink to an agar solution (corresponding approximately to an optical absorption coefficient  $\mu_a$  of  $1.2 \text{ cm}^{-1}$  at 680 nm). The background optical absorption and scattering were achieved by mixing India ink and intralipid with an agar solution. This corresponded to an approximate optical absorption coefficient  $\mu_a$  of  $0.1 \text{ cm}^{-1}$  at 680 nm and an approximate reduced scattering coefficient  $\mu_s'$  of  $7 \text{ cm}^{-1}$ . These values were chosen to approximate average light fluence attenuation in biological soft tissues [20–22]. This phantom was imaged at several optical wavelengths between 680 and 980 nm.

## 2.2.2 | In vivo datasets

All animal handling protocols were performed under supervision of trained personnel in accordance with institutional and local guidelines and with the approval of the Government of Upper Bavaria, Germany. Mice were housed in an animal housing facility ( $21 \pm 2$  °C,  $36\% \pm 2\%$  humidity) on a 12/12-h light/dark cycle at the Institute of Biological and Medical Imaging, Helmholtz Zentrum München (Munich, Germany). During the experiments, the mice were sedated (1.8% isoflurane in 100% O<sub>2</sub> at 0.81 ml/min) and immersed in a water bath kept at approximately 33 °C using a specialized mouse holder (iThera Medical GmbH, Munich, Germany).

To investigate the performance of the proposed PVC-wMB reconstruction algorithm in vivo when the acoustic reflector is localized within the same region as the optical chromophores, we used a dataset (hereinafter referred to as “dataset 1”) acquired previously by our research group from a BALB/c nude mouse (Charles River Laboratories, Boston, MA, USA) bearing a mammary tumor xenograft. The animal was injected in its backside with 4 T1 cells ( $8 \times 10^5$  cells; CRL-2539, American Type Cell Culture Collection, Manassas, VA), and the xenograft was allowed to grow for several days, until it reached a size of 100 mm<sup>3</sup>. Then the animal was injected intravenously with *Rhodobacter sphaeroides* ( $1 \times 10^9$  CFU) [23, 24]. At 24 h later, the torso region was imaged at 25 wavelengths between 680 and 920 nm. This anatomical section was chosen because the spine acts as a strong source of acoustic reflections within the chromophore region.

In order to investigate the performance of the PVC-wMB algorithm when the acoustic reflector surrounds the chromophores, we tested it on a dataset (hereinafter referred to as “dataset 2”) which our research group had previously acquired from the intact brain of a young adult mouse (Hsd:Athymic Nude-Foxn1nu/nu) at 805 nm. This wavelength was chosen because it is close to the isosbestic point for hemoglobin. In this case, the intact skull provided a strong acoustic reflector that surrounds the chromophores inside the brain. Further details about the experimental procedure can be found in the previous publication [25].

To demonstrate the additional advantage of the PVC-wMB algorithm of suppressing streaking artifacts arising from strong OA generation in the case of PV detection scenarios, we tested it on a dataset (hereinafter referred to as “dataset 3”) that we acquired from an 8-week-old female athymic Nude-Foxn1<sup>-/-</sup> mouse (Envigo, Huntingdon, UK) bearing a 4 T1 tumor. 4 T1 cells (American Type Culture Collection) were cultured in RPMI-1640 medium (Sigma) supplemented with 10% fetal bovine serum (Gibco) and 1% penicillin–streptomycin (Sigma). Cells ( $0.25 \times 10^6$ ) were inoculated orthotopically into the

right third thoracic mammary fat pad of the mouse, and allowed to grow for 15 days, until the tumor reached a diameter of 1 cm ( $\sim 0.5$  cm<sup>3</sup> in volume). The transversal section of the tumor with the longest diameter, corresponding to its anatomical center, was imaged on the last day (day 15) at 27 wavelengths between 700 and 960 nm. The skin on the tumor ulcerated on the day of imaging and consequently, coagulated blood on the surface of the ruptured skin produced a very strong OA signal, causing a severe streaking artifact. Although this ulceration was unintentional, it provided a good opportunity to evaluate the proposed PVC-wMB algorithm. It is important to note that this streaking artifact was not due to the presence of acoustic heterogeneities in the imaged sample, but rather due to the PV geometry itself.

## 2.3 | Quantitative and multispectral data analysis

As contrast is an important factor of determining whether a region can be differentiated from the background, we used the CNR measure to quantify the improvement achieved by the PVC-wMB reconstruction in the contrast of the upper boundary of the phantom that is particularly distorted by the wMB algorithm due to the PV detection geometry. The CNR is defined as follows: [26]

$$\text{CNR} = \frac{|\mu_{\text{ROI}} - \mu_{\text{BGD}}|}{\sqrt{\sigma_{\text{ROI}}^2 + \sigma_{\text{BGD}}^2}}, \quad (11)$$

where  $\mu_{\text{ROI}}$ ,  $\mu_{\text{BGD}}$  and  $\sigma_{\text{ROI}}$ ,  $\sigma_{\text{BGD}}$  are the means and standard deviations of a given ROI and BGD, respectively, both with homogenous intensities.

To demonstrate the spectral performance of the proposed PVC-wMB reconstruction algorithm, spectral unmixing was performed after acoustic reconstruction using linear least-squares spectral fitting for in vivo datasets 1 and 3 [27, 28]. This is a conventional spectral unmixing model in the OA literature, in which the measured spectrum at any pixel is assumed to be a linear combination of distinctive spectral components [29, 30]. For the multispectral datasets 1 and 3, oxy- and deoxy-hemoglobin spectral components were unmixed in image areas where reflection and streaking artifacts, respectively, were apparent. Then, oxygen saturation (sO<sub>2</sub>) values at the respective pixels were calculated based on the unmixed spectra.

## 3 | RESULTS

The performance of the proposed PVC-wMB reconstruction algorithm was compared with that of the

conventional MB algorithm and the unmodified wMB algorithm, first for the simplified case of the tissue-mimicking phantom (Figure 3), and then for the three in vivo datasets (Figure 4). Before investigating the results, it is important to know that the value of the heuristic parameter  $\omega$  was kept at 1 for all datasets investigated in this article, as it maintained the best compromise between mitigating artifacts (as will be shown later) and avoiding smearing the overall reconstruction for most cases, and also to focus more on studying the effect of the introduced Pvc. For more information about the effect of varying  $\omega$ , we refer the reader to the discussion in [11, 12], where the original statistical weighting scheme was first developed for the backprojection and MB reconstruction, respectively. Additionally for the in vivo dataset 3, we investigated the effect of reducing  $\omega$  on the smearing of structures in the center of the image that was induced by the weighting scheme.

### 3.1 | Phantom validation

The three algorithms were compared with regard to their ability to reconstruct the phantom shown in Figure 3a, containing an optical chromophore and a strong acoustic reflector. Figure 3b shows the OA reconstruction using the conventional MB algorithm, where typical arc-like

reflection artifacts (indicated by the red arrows) are noticeable. Figure 3c shows the OA reconstruction with the unmodified wMB algorithm, which mitigated the reflection artifacts but also caused severe distortion in the upper boundary of the phantom (enclosed by the dotted ellipse), which was not fully covered by the detection geometry. Figure 3d shows the reconstruction with the proposed Pvc-wMB algorithm, which recovered the upper distorted boundary of the phantom without compromising the capability of the wMB algorithm to mitigate the arc-like reflection artifacts. Figure 3e shows the intensity profile along the line  $l_1$  across the arc-like artifact in Figure 3b. The wMB weighting scheme by itself mitigated this artifact, and the proposed Pvc-wMB algorithm maintained this mitigation as well. Figure 3f shows the intensity profile along the line  $l_2$  across the upper edge of the phantom in Figure 3b. The proposed Pvc recovered this edge of the phantom that was visible in the conventional MB reconstruction in Figure 3b, reversing the distortion caused by the wMB algorithm in Figure 3c. Figure 3g shows the CNR values (calculated based on Equation 11) for the wMB and Pvc-wMB reconstructions acquired with different illumination wavelengths. The CNR was calculated taking into account that the ROI and BGD regions are those indicated by the light-yellow arc and light-red square, respectively, in Figure 3d. This ROI was particularly chosen because it represents the

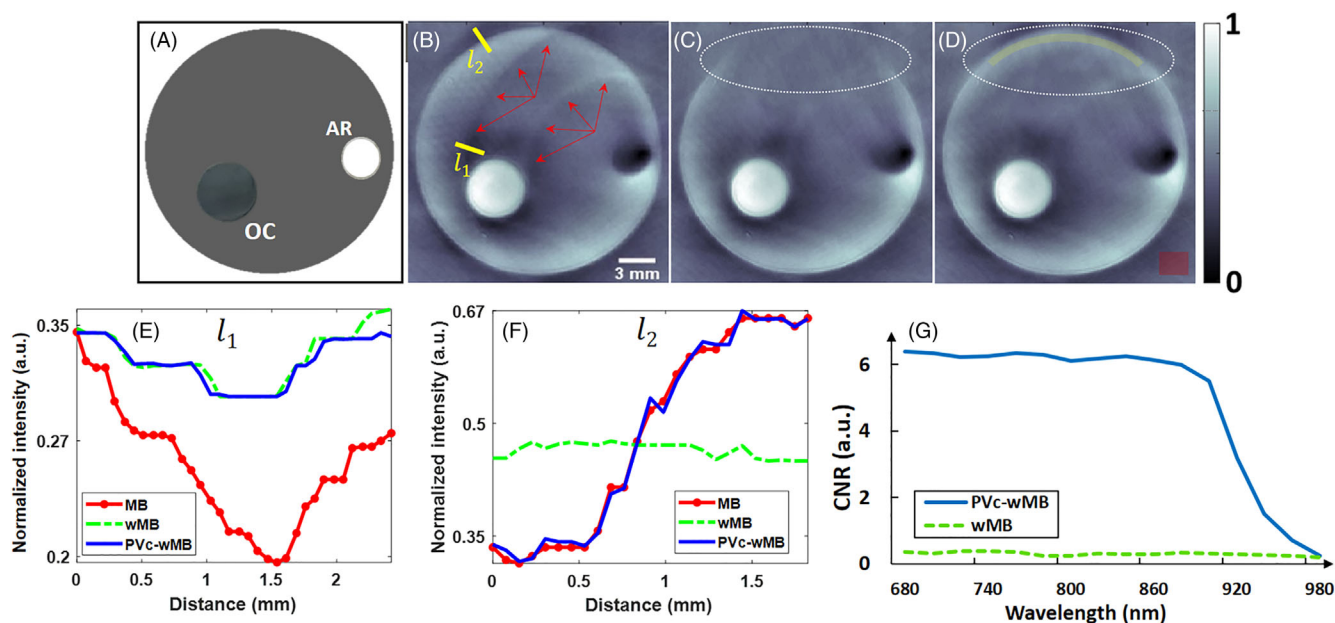


**FIGURE 3** Anatomical performance of the Pvc-wMB algorithm for the tissue-mimicking phantom. Upper row: (a) A schematic cross-section of the phantom. OC, optical chromophore; AR, acoustic reflector. (b–d) OA reconstruction of the phantom using (b) MB, (c) wMB, and (d) Pvc-wMB algorithms. Red arrows in (b) indicate typical arc-like reflection artifacts.  $l_1$  and  $l_2$  are lines taken for intensity profile analysis in (e) and (f), respectively. Dotted ellipses in (c) and (d) indicate the area not fully covered by the detection geometry. Light-yellow arc and light-red square in (d) indicate the ROI and BGD regions, respectively, used for CNR calculation in (g). Lower row: (e–f) Intensity profiles for lines (e)  $l_1$  and (f)  $l_2$  from (b). (g) CNR plots based on the ROI & BGD regions indicated in (d)

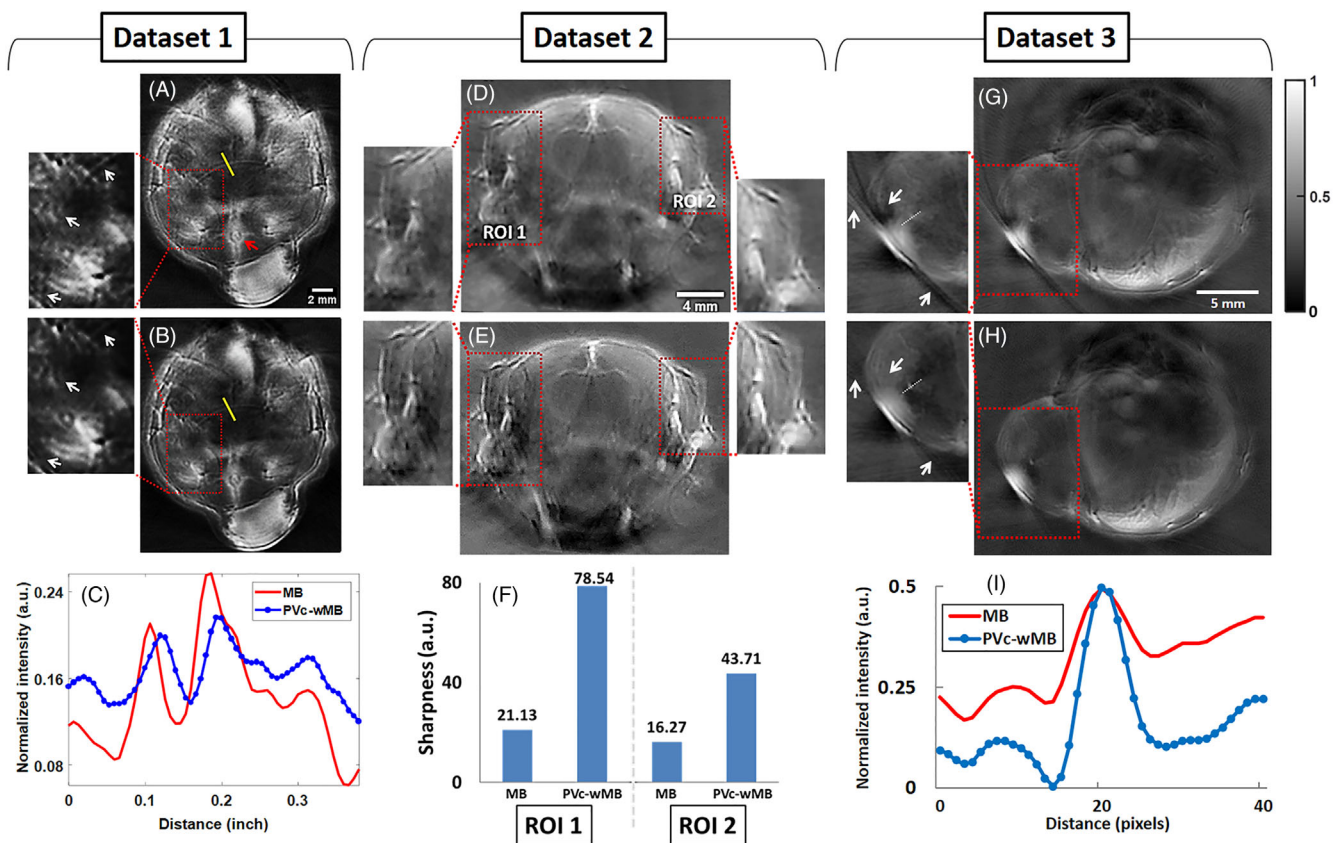


**FIGURE 4** Anatomical performance of the PVC-wMB algorithm for the three in vivo datasets. First column: OA reconstructions of dataset 1 using (a) MB and (b) PVC-wMB algorithms. The red arrow in (a) indicates the spine. White arrows in the side insets of (a) and (b) indicate typical reflection artifacts. (c) Intensity profile along the yellow line taken across the reflection artifact in (a) and (b). Second column: OA reconstructions of dataset 2 using (d) MB and (e) PVC-wMB algorithms. The side insets indicate two ROIs used for further sharpness analysis. (f) Sharpness measures of the two ROIs in (d) and (e). Third column: OA reconstructions of dataset 3 using (g) MB and (h) PVC-wMB algorithms. White arrows in the side insets indicate typical streaking artifacts due to the very strong OA generation by coagulated blood. (i) Intensity profile along the dotted line taken across the small vessel in the side insets of (g) and (h)

region with homogenous intensity (theoretically) that is particularly distorted by the wMB algorithm, but recovered by the PVC-wMB algorithm. As shown in Figure 3g, the PVC-wMB algorithm maintains a considerably higher CNR for most of the wavelength range, compared with the wMB algorithm alone. The steep drop of the CNR for the PVC-wMB reconstructions starting around 890 nm is due to the fact that the increasing optical absorption of water starts to significantly affect the overall reconstruction quality as the image becomes much noisier and contrast is lost all over the image.

### 3.2 | In vivo validation

Next, we compared the performance of the PVC-wMB algorithm with that of the conventional MB algorithm for reconstructing OA in vivo data. Figure 4 shows the three datasets, each presenting a different challenge for accurate OA reconstruction.

In dataset 1, the spine (indicated with the red arrow in Figure 4a) acts as a strong acoustic reflector inside the mouse. Comparison of the magnified insets of Figure 4a and b shows that the proposed PVC-wMB algorithm mitigates the reflection artifact (indicated by the white arrows). Figure 4c confirms this mitigation by showing less intensity variations along the yellow profile line across the reflection artifact in (a) and (b). This mitigation of the reflection artifact was achieved without causing distortion of the upper part of the image, which was not fully covered by the detection geometry.

In the case of dataset 2, the skull acted as a strong acoustic reflector surrounding the OA chromophores. Visual inspection of Figure 4d and e and the two magnified ROIs demonstrates that the PVC-wMB reconstruction has qualitatively a higher overall sharpness. Figure 4f confirms this increase of sharpness quantitatively based on the Brenner's gradient of sharpness [31].

In dataset 3, a blood vessel within the tumor ruptured near the skin and released blood that coagulated, creating

a strongly absorbing chromophore that gave rise to streaking artifacts in the subsequent OA reconstruction. Although such streaking artifacts arise from the PV detection geometry itself and not from acoustic heterogeneities, the proposed PVC-wMB algorithm was able to suppress them as well. Comparison of Figure 4g and h demonstrates that the proposed algorithm significantly suppressed the streaking artifacts around the coagulated blood (indicated with the white arrows), again without introducing distortion in the upper image part which was not fully covered by the detection geometry. This streaking suppression led to enhancing the delineation of the tumor boundary. Figure 4i shows the intensity profile across a blood vessel within the tumor (indicated with the small dotted line in the magnified insets of (g) and (h)), further demonstrating the ability of the proposed algorithm to reproduce fine anatomical details with relatively higher contrast.

For dataset 3, however, it has to be noted that the PVC-wMB reconstruction for  $\omega = 1$  caused slight smearing of some of the image parts in the center. This smearing can be better visualized in Figure 5d, which shows the absolute difference image between the MB reconstruction (Figure 4g) and the PVC-wMB reconstruction for  $\omega = 1$  (Figure 4h, also shown in Figure 5a). A similar smearing of some of the image parts in the center

for the small animal imaging results was also reported in Reference [11] (where the statistical weighting scheme was first introduced to backprojection reconstruction). There, the smearing started to become noticeable with values of  $\omega$  more than 1. Reducing the value of  $\omega$  can reduce such smearing. For our in vivo dataset 3, and in comparison with Figure 5d, this reduction of smearing can be noticed in Figure 5e and f, which are the difference images between the MB reconstruction and the PVC-wMB reconstructions for  $\omega = 0.8$  (Figure 5b) and  $\omega = 0.5$  (Figure 5c), respectively. This reduction of smearing for  $\omega$  values  $< 1$  is attained while still maintaining acceptable suppression of the streaking artifact around the ulceration area. It has to be pointed out that because  $\omega$  is a heuristic parameter, and also due to the statistical nature of the weighting scheme, it is up to the user to select the value of  $\omega$  that achieves the best compromise between mitigating artifacts and maintaining minimal smearing of true image information for any given dataset.

### 3.2.1 | Validation of spectral unmixing

The results for in vivo reconstruction suggest that the PVC-wMB algorithm can improve the anatomical quality of reconstructed images. We further investigated whether

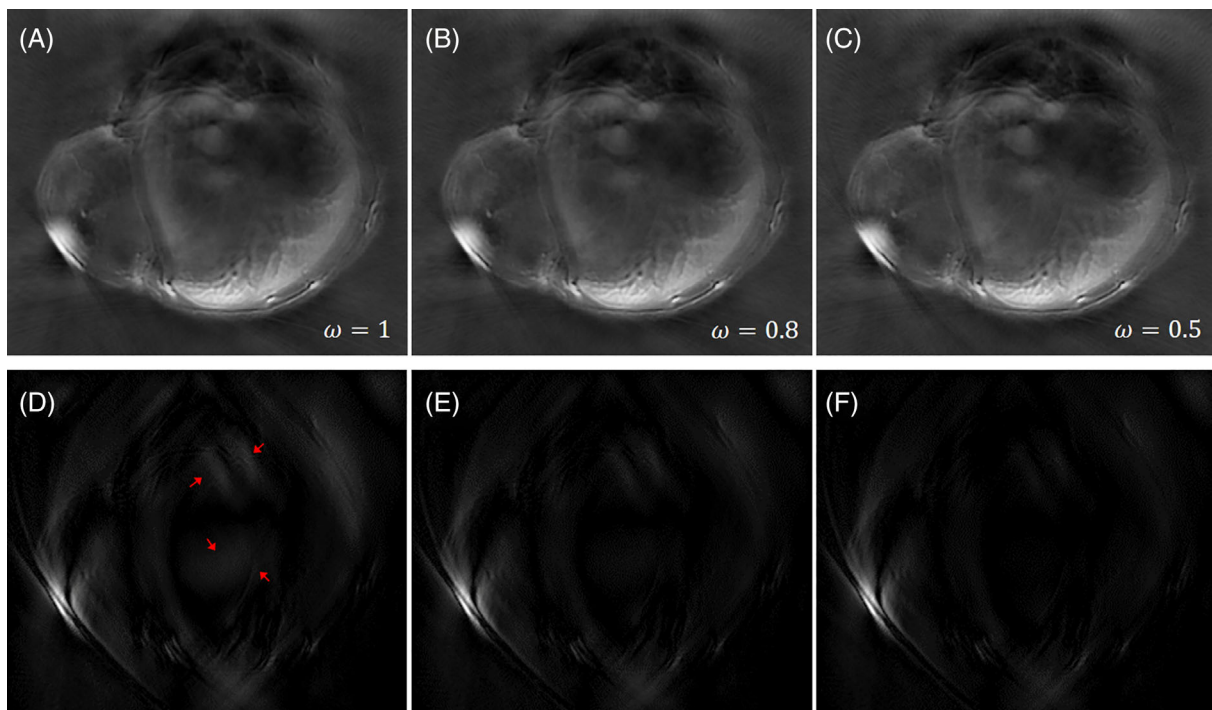


**FIGURE 5** Effect of reducing  $\omega$  on the appearance of internal parts for the in vivo dataset 3. Upper row: PVC-wMB reconstructions at (a)  $\omega = 1$ , (b)  $\omega = 0.8$ , and (c)  $\omega = 0.5$ . Lower row: Absolute difference images between the MB reconstruction (Figure 4(g)) and the PVC-wMB reconstructions at (d)  $\omega = 1$ , (e)  $\omega = 0.8$ , and (f)  $\omega = 0.5$ . Red arrows in (d) indicate internal parts that were slightly smeared in (a). Such smearing was reduced by reducing  $\omega$  as can be noticed in (e) and (f)

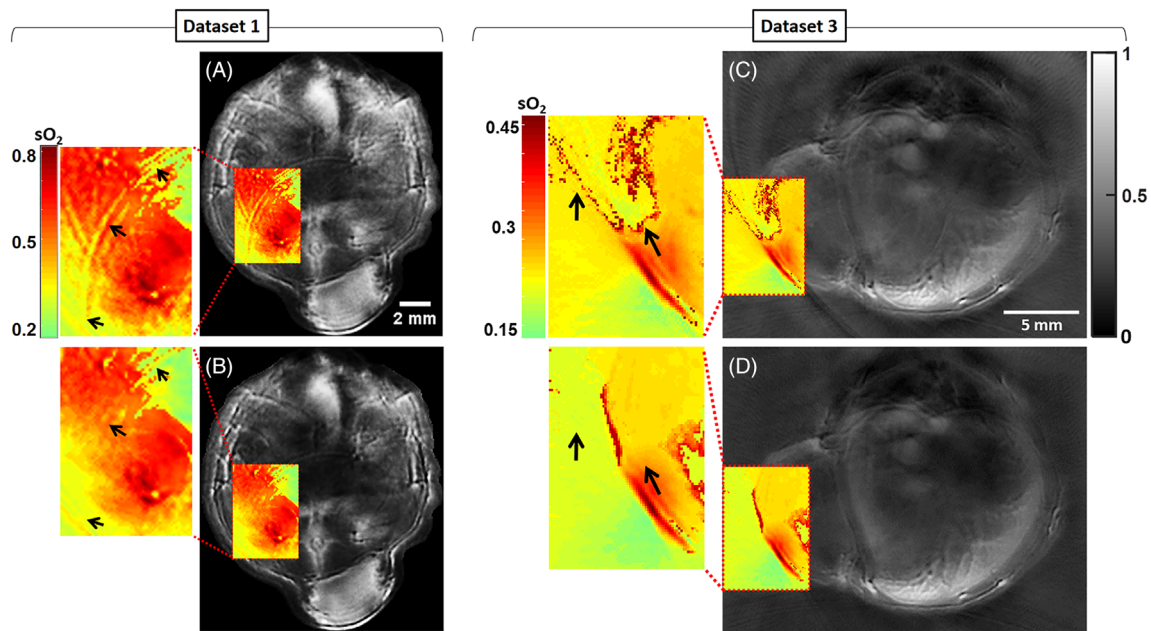


**FIGURE 6** Spectral unmixing performance of the PVC-wMB reconstruction for two in vivo datasets. Left column: Overlay of spectral unmixing ( $sO_2$  map) of an ROI on reconstructions of dataset 1 using (a) MB, and (b) PVC-wMB algorithms. The side insets show zoomed images of the ROI affected by the reflection artifact. Black arrows in the insets indicate  $sO_2$  signatures of reflection artifacts. Right column: Overlay of spectral unmixing ( $sO_2$  map) of an ROI on reconstructions of dataset 3 using (c) MB, and (d) PVC-wMB algorithms. The side insets show zoomed images of the ROI affected by the streaking artifact. Black arrows in the insets indicate  $sO_2$  signatures of the streaking artifacts

the proposed method could improve spectral unmixing results in order to generate more reliable mapping of functional measures such as the  $sO_2$ . Hence, we compared the spatial estimation of  $sO_2$  in areas of the abovementioned mouse tumor images showing a reflection artifact (dataset 1) and a streaking artifact (dataset 3). Comparison of Figure 6a and b indicates that the PVC-wMB mitigated the spectral signature of the reflection artifact observed in the conventional MB reconstruction (indicated by the black arrows in the side insets). Similarly, comparison of Figure 6c and d shows that the PVC-wMB also suppressed the spectral signature of the streaking artifact (indicated by the black arrows in the side insets), thus enhancing the delineation of the spectral signature of the tumor, similar to what was observed anatomically in Figure 4h.

## 4 | DISCUSSION AND CONCLUSION

In this article, we modified the wMB reconstruction algorithm to have a better performance for PV geometries. The proposed PVC-wMB algorithm showed generally better reconstruction performance compared with both the conventional MB and the unmodified wMB algorithms.

For both phantom and in vivo data, the PVC-wMB retained the ability of the wMB algorithm to mitigate reflection and/or streaking artifacts observed with conventional MB reconstruction. Additionally, the proposed method did not introduce distortions observed with the wMB algorithm in areas not fully enclosed by the detection geometry. The proposed PVC-wMB algorithm was found to have better performance at the anatomical as well as spectral level, potentially allowing for more reliable estimation of functional parameters like  $sO_2$  for in vivo measurements. The proposed reconstruction scheme can support a more accurate and reliable preclinical and clinical analysis using commercially available MSOT imaging systems, most of which feature PV geometries.

In the case of an acoustic reflector localized inside the imaged target, we observed in experiments with a tissue-mimicking phantom and an in vivo dataset (dataset 1) that the PVC-wMB reconstruction algorithm mitigates the reflection artifacts without giving rise to the distortion caused by the weighting scheme of the unmodified wMB algorithm. While imaging a tumor xenografted on a mouse in vivo (dataset 3), we also observed the additional advantage of the proposed algorithm to suppress typical streaking artifacts around super strong absorbers due to the PV geometry itself [32]. It is worth mentioning that

such streaking patterns are similar to the undersampling artifacts caused by spatial aliasing in x-ray CT [33]. Such artifacts are significantly aggravated when a structure of an extraordinary intensity that is outside the normal range is present in the field of view. This likely increases the ill-posedness of the tomographic inversion problem for PV geometries and manifests itself as such strong streaking. For example, the presence of metal implants causes severe streaking patterns around them in x-ray CT [33]. Similarly for our OA in vivo dataset 3, the coagulated blood acted as a “super” chromophore whose intensity is unmatched by other chromophores in the image, leading to streaking around it. That is why such streaking was particularly apparent in this in vivo dataset. Suppression of such streaking artifacts is of profound importance in cases where strong OA chromophores (e.g., black moles) are present on the skin of animals, such as B6 mice which are widely used in brown fat studies [34]. These spots generate strong OA signals accompanied with streaking patterns that smear the entire image and hinder its interpretability.

Figure 3 generally demonstrated the improvement by the PVC-wMB algorithm for reconstructing the tissue-mimicking phantom. It can be noticed however that the upper-left boundary of the acoustic reflector was poorly delineated in all reconstruction results. The reason for this is the PV geometry itself. That is; OA signals originating from background chromophores which are in the immediate neighborhood of this area did not propagate directly to any detector due to the absence of detectors on the 90° upper section of the detection arc (as in Figure 2a). Consequently, this led to loss of contrast at that part of the image. A solution for this issue is to employ a full-view detection geometry (i.e., 360°) to capture the full shape of the reflector. Another solution is to utilize acoustic a priori about the locations and shapes of strong acoustic heterogeneities during the reconstruction [35].

Perhaps an even more stringent test of the PVC-wMB algorithm was its ability to enhance the reconstruction of images of an entire mouse brain in vivo through the intact skull (dataset 2). In this case, the acoustic reflector surrounds the chromophores. The PVC-wMB algorithm enhanced the overall sharpness of the reconstructed image. This increase in sharpness likely reflects the algorithm's ability to mitigate reflection artifacts caused by the skull. As a result, the detected OA signals had less ambiguity, and image features, which have apparently been blurred by the reflection artifacts, could be more accurately reconstructed and localized. This enhancement in the quality of the reconstruction was achieved without introducing distortions to the upper part of the image which was not well covered by the detection geometry. Such enhancement

can further facilitate preclinical OA investigation of the brain activity through the intact skull, which is a main challenge in in vivo transcranial imaging [36].

The improvement in anatomical imaging performance was accompanied by enhanced spectral unmixing results for the in vivo datasets 1 and 3, potentially leading to more reliable sO<sub>2</sub> estimates and better differentiation between normal and malignant tissue. However, for a more rigorous analysis of the effect of the proposed algorithm on spectral unmixing, tissue-mimicking phantom experiments with dyes having unique spectral signatures (e.g., Indocyanine green) would be required so that a “ground-truth” spectral map can be established, to which results can be reliably compared. Such analysis is planned for future work.

Overall, the proposed PVC-wMB algorithm achieved better reconstruction results in comparison with the conventional MB algorithm by mitigating reflection and/or streaking artifacts. This enhancement was achieved without sacrificing reconstruction quality and causing distortions in image sections not fully enclosed by the PV detection geometry, in comparison with the unmodified wMB algorithm. Additionally, the proposed PVC-wMB algorithm maintains the inherent advantage of the wMB algorithm of not requiring prior knowledge of the exact locations or distribution of OA chromophores or acoustic heterogeneities, thus giving it a wide variety of applications [12]. However, it may be possible to further improve its reconstruction performance by including such priors. The same statistical weighting scheme applied in the wMB algorithm was previously integrated into a back-projection reconstruction procedure that took into account the locations of strong acoustic heterogeneities as acoustic priors [37]. The inclusion of such priors enhanced the mitigation of reflection artifacts compared with the case where no priors were integrated. Therefore, we expect that the proposed PVC-wMB algorithm may also benefit from taking into account optical and acoustic priors in order to mitigate reflection and/or streaking artifacts more effectively. Another potential issue for future investigation is to compare the PVC-wMB algorithm with other non-negative reconstruction approaches [38, 39] particularly for the ability to suppress streaking artifacts in PV detection geometries.

In conclusion, in this article, we demonstrated that augmenting the wMB OA reconstruction algorithm with a correction scheme enhances its performance for PV geometries. The augmented algorithm has the potential to increase the quality of preclinical and clinical MSOT applications, such as tumor imaging and non-invasive brain imaging. The ability of the proposed algorithm to improve the reconstruction of not only anatomical but also functional information can further support the integration of OA imaging into research and clinical workflows.

## ACKNOWLEDGMENTS

This project has received funding from the European Commission under Grant Agreement No. 605162 (BERTI) and the European Union's Horizon 2020 research and innovation program under grant agreement no. 694968 (PREMSOT). Dr. Jaya Prakash acknowledges Alexander von Humboldt Postdoctoral Fellowship program. The authors wish to sincerely thank Dr. Xosé Luís Deán-Ben for his valuable inputs about the methodology of the wMB reconstruction algorithm. We would also like to thank Dr. Andre Stiel and Ivan Olefir for providing us with two in vivo datasets. Finally, we thank Dr. A. Chapin Rodriguez and Dr. Robert Wilson for their valuable comments on the manuscript. Open Access funding enabled and organized by Projekt DEAL.

## CONFLICTS OF INTEREST

The authors declare no conflict of interest.

## DATA AVAILABILITY STATEMENT

The data that support the findings of this study are available from the corresponding author upon reasonable request.

## ORCID

Marwan Muhammad  <https://orcid.org/0000-0002-6119-1686>

Jaya Prakash  <https://orcid.org/0000-0002-2375-154X>

## REFERENCES

- [1] R. A. Kruger, P. Liu, Y. Richard Fang, C. R. Appledorn, *Med. Phys.* **1995**, *22*, 1605.
- [2] Y. Xu, L. V. Wang, *Phys. Rev. Lett.* **2004**, *92*, 033902.
- [3] L. V. Wang, *Photoacoustic Imaging and Spectroscopy*, CRC Press, Boca Raton **2009**.
- [4] X. L. Den-Ben, D. Razansky, V. Ntziachristos, *Phys. Med. Biol.* **2011**, *56*, 6129.
- [5] X. L. Deán-Ben, V. Ntziachristos, D. Razansky, *Med. Phys.* **2014**, *41*, 073301.
- [6] X. Jin, C. Li, L. V. Wang, *Med. Phys.* **2008**, *35*, 3205.
- [7] C. Li, L. V. Wang, *Phys. Med. Biol.* **2009**, *54*, R59.
- [8] P. Vaupel, *Oncologist* **2004**, *9*, 4. <https://doi.org/10.1634/theoncologist.9-90005-4>.
- [9] D. Modgil, M. A. Anastasio, P. J. La Rivière, *J. Biomed. Opt.* **2010**, *15*, 021308.
- [10] H. Jiang, Z. Yuan, X. Gu, *J. Opt. Soc. Am. A* **2006**, *23*, 878.
- [11] X. L. Deán-Ben, R. Ma, D. Razansky, V. Ntziachristos, *IEEE Trans. Med. Imaging* **2011**, *30*, 401.
- [12] X. L. Deán-Ben, R. Ma, A. Rosenthal, V. Ntziachristos, D. Razansky, *Phys. Med. Biol.* **2013**, *58*, 5555.
- [13] A. Rosenthal, D. Razansky, V. Ntziachristos, *IEEE Trans. Med. Imaging* **2010**, *29*, 1275.
- [14] M. A. Anastasio, J. Zhang, X. Pan, Y. Zou, G. Ku, L. V. Wang, *IEEE Trans. Med. Imaging* **2005**, *24*, 199.
- [15] Y. Xu, L. V. Wang, G. Ambartsoumian, P. Kuchment, *Med. Phys.* **2004**, *31*, 724.
- [16] V. Neuschmelting, N. C. Burton, H. Lockau, A. Urlich, S. Harmsen, V. Ntziachristos, M. F. Kircher, *Photoacoustics* **2016**, *4*, 1.
- [17] X. L. L. Deán-ben, V. Ntziachristos, D. Razansky, *IEEE Trans. Med. Imaging* **2012**, *31*, 1154.
- [18] D. Razansky, A. Buehler, V. Ntziachristos, *Nat. Protoc.* **2011**, *6*, 1121.
- [19] A. Dima, N. C. Burton, V. Ntziachristos, *J. Biomed. Opt.* **2014**, *19*, 036021.
- [20] S. L. Jacques, *Phys. Med. Biol.* **2013**, *58*, 37.
- [21] P. Di Ninni, F. Martelli, G. Zaccanti, *Opt. Express* **2010**, *18*, 26854.
- [22] P. Lai, X. Xu, L. V. Wang, *J. Biomed. Opt.* **2014**, *19*, 035002.
- [23] Paustian, T. D. & Kurtz, R. S. Transposon mutagenesis of *Rhodobacter sphaeroides*. Proceedings of the 15th Workshop of the Association for Biology Laboratory Education 15 45–61 (**1994**).
- [24] J. F. Imhoff, H. G. Trüper, N. Pfennig, *Int. J. Syst. Bacteriol.* **1984**, *34*, 340.
- [25] F. Timischl, *Scanning* **2015**, *37*, 54.
- [26] I. Olefir, E. Mercep, N. C. Burton, S. V. Ovsepian, V. Ntziachristos, *J. Biomed. Opt.* **2016**, *21*, 086005.
- [27] E. Herzog, A. Taruttis, N. Beziere, A. A. Lutich, D. Razansky, V. Ntziachristos, *Radiology* **2012**, *263*, 461.
- [28] D. Razansky, M. Distel, C. Vinegoni, R. Ma, N. Perrimon, R. W. Köster, V. Ntziachristos, *Nat. Photonics* **2009**, *3*, 412.
- [29] S. Tzoumas, A. Nunes, I. Olefir, S. Stangl, P. Symvoulidis, S. Glasl, C. Bayer, G. Multhoff, V. Ntziachristos, *Nat. Commun.* **2016**, *7*, 1.
- [30] S. Tzoumas, N. Deliolanis, S. Morscher, V. Ntziachristos, *IEEE Trans. Med. Imaging* **2013**, *33*, 48.
- [31] B. E. Treeby, T. K. Varslot, E. Z. Zhang, J. G. Laufer, P. C. Beard, *J. Biomed. Opt.* **2011**, *16*, 090501.
- [32] J. Friel, E. T. Quinto, *SIAM J. Appl. Math.* **2014**, *75*, 703.
- [33] J. F. Barrett, N. Keat, *Radiographics* **2004**, *24*, 1679.
- [34] A. Vitali, I. Murano, M. C. Zingaretti, A. Frontini, D. Ricquier, S. Cinti, *J. Lipid Res.* **2012**, *53*, 619.
- [35] H. Yang, D. Jüstel, J. Prakash, A. Karlas, A. Helfen, M. Masthoff, M. Wildgruber, V. Ntziachristos, *Photoacoustics* **2020**, *19*, 100172.
- [36] H. Estrada, J. Rebling, J. Turner, M. Kneipp, S. Shoham, D. Razansky, Estimation of the skull insertion loss using an opto-acoustic point source. in *International Society for Optics and Photonics*, Vol. 9708 (Eds: A. A. Oraevsky, L. V. Wang), Society of Photo-Optical Instrumentation Engineers, Bellingham, WA **2016**, 97080M.
- [37] X. L. Deán-Ben, V. Ntziachristos, D. Razansky, *Appl. Phys. Lett.* **2011**, *98*, 171110.
- [38] J. Prakash, S. Mandal, D. Razansky, V. Ntziachristos, *I.E.E.E. Trans. Biomed. Eng.* **2019**, *66*, 1. <https://doi.org/10.1109/TBME.2019.2892842>.
- [39] L. Ding, X. Luís Deán-Ben, C. Lutzweiler, D. Razansky, V. Ntziachristos, *Phys. Med. Biol.* **2015**, *60*, 6733.

**How to cite this article:** M. Muhammad, J. Prakash, E. Liapis, V. Ntziachristos, D. Jüstel, *J. Biophotonics* **2022**, e202100334. <https://doi.org/10.1002/jbio.202100334>